

# Curved-array-based Multispectral Photoacoustic Imaging of Human Finger Joints

Na Huang, Ming He, Haosheng Shi, Yuan Zhao, Man Lu, Xianbing Zou, Lei Yao, Huabei Jiang, and Lei Xi\*

**Abstract— Objective:** In this study, we present the design, fabrication, and evaluation of a curved-array-based photoacoustic imaging system designed for imaging vasculatures inside human finger joints with multispectral strategy. **Methods:** The transducers was fabricated with polyvinylidene fluoride (PVDF) film with a size of 30 mm×2.8 mm, and a curvature radius of 82 mm. A detailed comparison between the PVDF transducer and commercial piezoelectric ceramic (PTZ) transducers was performed. In addition, phantom and *in vivo* mouse experiments were carried out to evaluate the system performance. Furthermore, we recruited healthy volunteers and did multispectral photoacoustic imaging of blood vessels in finger joints. **Results:** The transducers have an average center frequency of 6.6 MHz, and a mean bandwidth of 95%. The lateral and axial resolutions of the system are 110  $\mu\text{m}$  and 800  $\mu\text{m}$ , respectively, and the diameter of the active imaging is larger than 50 mm. We successfully captured the drug-induced cerebral bleeding spots in intact mouse brains, and recovered both morphology and oxygen saturation of the blood vessels in human finger joints. **Conclusions:** The PVDF transducer has a better performance in bandwidth compared with commercial transducers. The curved design of the transducer offers a better sensitivity and a higher axial resolution compared with the flat design. **Significance:** Based on the phantom, animal and human experiments, the proposed system has the potential to be used in clinical diagnosis of early-stage arthritis.

**Index Terms—**Photoacoustic imaging, functional photoacoustic computed tomography, array-based photoacoustic system, arthritis.

This work was supported in part by National Natural Science Foundation of China under Grant 81571722 and Grant 61528401, in part by State International Collaboration Program from Sichuan under Grant 2016HH0019, and also supported in part by University of Electronic Science and Technology of China under startup grant A03012023601011. *Asterisk indicates corresponding author.*

N. Huang, M. He, Y. Zhao and L. Yao are with the School of Physical Electronics, University of Electronic Science and Technology of China.

H. Shi and X. Zou are with the National Key Laboratory of Science and Technology on Communications, University of Electronic Science and Technology of China.

M. Lu is with the School of Medicine, University of Electronic Science and Technology of China, and Department of Ultrasound, Sichuan Cancer Hospital Institute, Chengdu, Sichuan 610047, China.

H. Jiang is with the School of Physical Electronics, the Center for Information in Medicine, University of Electronic Science and Technology of China, and Department of Medical Engineering, University of South Florida, Tampa, FL 33620 USA.

\*L. Xi is with the School of Physical Electronics, and the Center for Information in Medicine, University of Electronic Science and Technology of China, Chengdu, Sichuan 610054, China (e-mail: xilei1985@uestc.edu.cn).

## I. INTRODUCTION

ARTHRITIS affects millions of people in the world and remains the leading cause of disability in the people over 50-year [1], [2]. Osteoarthritis (OA) and rheumatoid arthritis (RA) are two major types of arthritis. Based on the clinical observation, distal interphalangeal (DIP) joints and proximal interphalangeal (PIP) joints reveal symptoms such as swelling, stiffness and pain in the early stage of arthritis [3]-[5]. Intervention in the early stage of arthritis will significantly provide the best protection of the joint functions [6], [7]. However, it is challenging for current clinical imaging modalities such as X-ray imaging, magnetic resonance imaging (MRI) and ultrasound imaging (US) to diagnose early-stage arthritis due to their inherent limitations such as ionizing radiation of X-ray, high cost and low temporal resolution of MRI, and low contrast of US [8]-[10].

Optical imaging techniques, such as near-infrared spectroscopy (NIRS) and diffuse optical tomography (DOT), have been proposed to diagnose both OA and RA in the early stage due to their merits of deriving both functional and morphological parameters [11]-[14]. However, they suffer from low spatial resolution, and thus require additional prior information from other complementary techniques such as X-ray tomosynthesis and MRI [15], [16].

Photoacoustic imaging (PAI), a promising imaging technology, has evolved rapidly during the past decades [17]. It is a hybrid imaging modality that owns rich optical contrast, deep tissue penetration depth and high acoustic resolution [18], [19]. Photoacoustic computed tomography (PACT), a macroscale sub-modality of PAI, is a reconstruction-based imaging technique, and has a submillimeter spatial resolution and a typical penetration depth of centimeters. It has demonstrated various applications in biomedicine and clinics [20]-[25]. For the first time, Wang *et al.* used a conventional two-dimensional (2D) PACT to image subcutaneous tissues and phalanx of PIP and DIP joints in a hand amputated from a female cadaver [20]. Jiang *et al.* proposed a quantitative spherical-scanning-based PACT system to recover both structural and functional parameters of finger joints in arthritis patients [22]. Xi *et al.* combined the concept of virtual detector with a spherically focused transducer to reconstruct soft tissues, ligaments and phalanx of the DIP joint in three-dimension, and further integrated PACT with DOT to obtain additional scattering properties of the DIP joint [23], [24]. Li *et al.* built a

multi-transducer-based PACT system using a new acoustic/optical combiner to image the blood vessels in the DIP joint of healthy volunteers [25].

These conventional PACT systems utilize the scanning of either the transducer or the sample [26]. They require a long experimental time to complete a circular/semi-spherical scanning, and thus are not suitable for clinical applications. It is feasible to improve the temporal resolution by using a high-repetition laser. However, beside the expensive cost, high-repetition laser is not suitable for deep-tissue imaging due to the low pulse energy. Apart from the utilization of a fast laser, using an array-based PACT system is an alternative way to achieve high-speed imaging. Gamelin *et al.* reported a 128-channel PACT system with a curved quarter-ring configuration. They successfully obtained the *ex vivo* images of mouse brain within 15 seconds through rotating the sample [27]. In the second generation, they developed a 512-element full-ring array to achieve fast two-dimensional (2D) imaging with a maximum speed of 8 frames per second (fps) [28]. Yang *et al.* applied a 128-element linear array system to visualize the vascular network in the rat brain [29]. Jiang group developed a full-ring array-based PACT system using 192 single transducers to study the hemodynamics of mouse brain during the onset of epilepsy, and further extended the 2D array to a spherical 3D array [30], [31]. Brecht *et al.* has developed a 3D photoacoustic tomography system based on a concave arc-shaped array of 64 piezocomposite transducers. They demonstrated the whole-body imaging of a mouse with a spatial resolution of 0.5 mm [32]. Kruger and his colleagues described a bowl-shaped transducer array to recover the 3D vascular network in healthy human breasts [33]. To obtain sufficient temporal resolution for clinical imaging of human finger joints, Manohar *et al.* built a curvilinear 32-element photoacoustic array to detect the blood vessels inside the DIP and PIP joints, which are associated with early development of RA [34]. Razansky *et al.* successfully visualized the perfusion of indocyanine green (ICG) in the blood vessels of human finger joints using a 128-element-based photoacoustic imaging system [35]. Wang *et al.* modified a clinical ultrasound imaging system and achieved dual-modality photoacoustic and ultrasound imaging of joint structures and functions [36].

Apart from above systems, several groups have developed 2D/3D array-based PACT systems using polyvinylidene fluoride (PVDF) film and successfully applied the system for breast cancer detection [15], [37]-[39], and functional brain studies [40]. PVDF, a type of polymer piezoelectric materials, has a lower acoustic impedance and a broader bandwidth compared to the ceramic counterparts. In addition, it is cheap, light-weight, flexible and easily integrated. However, the flat design of PVDF transducers leads to a lower sensitivity and a poor axial resolution. To improve both the signal to noise ratio (SNR) and axial resolution of previous PVDF-array-based systems, we developed a 60-element curved PVDF transducer array with a size of 30 mm×2.8 mm, and a curvature radius of 82 mm. Furthermore, the rotational scanning mechanism of the transducer array allows to acquire data in multiple detector positions, leading to a better image quality compared with

previous systems. In addition to phantom experiments, we applied this system to monitor the bleeding spot in intact mouse brains with drug-induced cerebral hemorrhage, and further demonstrated its feasibility in visualizing both structures and oxygen saturation of blood vessels in human finger joints.

## II. METHODS

### A. Fabrication of transducer array

We used flexible PVDF films (110µm-Ag-Ink Film, Measurement Specialties Inc., Hampton, VA) coated with silver electrodes in both sides. The film was reshaped into 60 rectangle pieces with an active area of 30 mm×2.8 mm. As shown in Figure 1a, the rectangular film was attached to the curved surface of a copper shielding case with a curvature radius of 82 mm to form a cylindrically focused detection. The positive and negative electrodes of the film were connected to a coaxial cable using the conductive epoxy. Then we poured the epoxy (EPO-TEK 301-2, Epoxy Tech., Billerica, MA) into the inside cavity of the shielding case serving as the backing material. We made a total number of 60 single element transducers and aligned them symmetrically in a ring-shaped resin holder that had an inside radius of 82 mm as shown in Figure 1b.

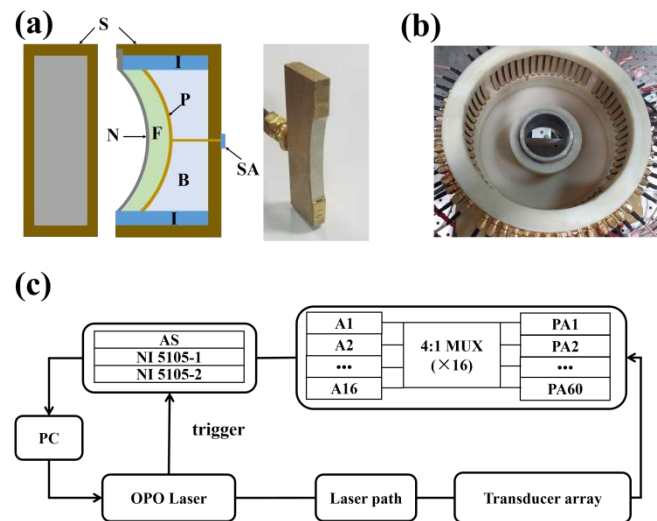


Fig. 1. Schematics and photographs of the fabricated transducer array and diagram of system configuration. (a) The schematics of a single PVDF transducer in front (left) and side (middle) views, and the photograph (right) of a completed PVDF transducer. (b) The photograph of the aligned array system. (c) The diagram of the system. N: negative electrode P: positive electrode F: 110 µm PVDF film S: shielding case B: backing material SA: SMA adaptor I: insulator PA: pre-amplifier A: amplifier MUX: multiplexer AS: acquisition system.

### B. System configuration

In Figure 1c, a Q-switched Nd: YAG laser (Q-smart 450, Quantel Laser) pumped an OPO laser (Magic Prism, Opotek Inc.) to generate laser pulses with a variable duration of 5~10 nanosecond (ns), and a maximum repetition rate of 20 Hz. The laser pulses were delivered to the mouse head and the surface of human finger joints via two different light delivery systems. The generated wideband photoacoustic signals were averaged 20 times, collected by the array, and amplified by 60 homemade low-noise preamplifiers at ~20 dB. The transducers

in the array were equally divided into four groups and sequentially selected by a multiplexer (PXI-2576, National Instruments Corp., TX), further amplified by additional 15 low-noise amplifiers at ~28 dB (ZFL-500LN, Mini Circuits Corp., NY), and digitalized by two 8-channel high-resolution data acquisition cards (PXI-5105, National Instruments Corp., TX) with a 20 MHz low-pass filter at a sampling rate of 60 MS/s. We rotated the entire imaging array twice with an angular step of  $2^\circ$  to obtain 180 detectors for one 2D image via a motorized rotator (RAP-125, Zolix Instruments CO., LTD, BJ), and did axial scanning with a step of 0.8 mm using a motorized elevator (PSAV-100-ZF, Zolix Instruments CO., LTD, BJ). The total experimental time for each 2D image is 15 s.

### C. System evaluation and calibration

#### 1) Frequency response

We evaluated the frequency response of each transducer using an impulsive wave method. As illustrated in Figure 2a, a transducer was immobilized in a water tank and connected to a broadband ultrasonic pulse/receiver (5073PR, Olympus Inc., MA). A stainless steel plate was positioned in front of the transducer and fixed on a manual linear stage. The pulse/receiver was set in the pulse-echo mode, drove the transducer to generate acoustic waves, and then received the echoes reflected by the stainless steel plate. We precisely adjusted the position of the plate and recorded the echoes with the highest amplitudes. We did Fourier transform of the gathered data, derived the center frequency and -6 dB bandwidth.

#### 2) Resolution evaluation

To investigate the best axial resolution of this system, we mapped the acoustic distribution of the transducer using the system depicted in Figure 2b. A short carbon fiber with a diameter of  $7\ \mu\text{m}$  and a length of  $100\ \mu\text{m}$  was vertically inserted in the center of a background phantom made by mixing the India ink, intralipid and agar. The background phantom had an optical absorption coefficient of  $0.01\ \text{mm}^{-1}$  and an optical scattering coefficient of  $1.0\ \text{mm}^{-1}$ . The phantom was immersed in a water tank and fixed on a 3D motorized linear stage (TSA-100, Zolix Instruments CO., LTD, BJ). A liquid optical fiber was utilized to deliver the excitation laser beam to the carbon fiber and moved with the phantom during the scanning. In the experiment, we first optimized position of the carbon fiber to the focal plane of the transducer, and then scanned a rectangular area of  $8\ \text{mm} \times 30\ \text{mm}$  in X-Z plane with an interval step of 0.1 mm. To reconstruct the acoustic distribution map, we did Hilbert transform of the raw photoacoustic signals, derived and directly back-projected the peak values. The full width at half maximum (FWHM) of the vertical profile at the focal length of the transducer was considered as the best axial resolution of the system.

#### 3) Phantom experiments

Several phantom experiments were conducted to estimate the lateral resolution of the system, and compared the PVDF transducer with two commercial lead titanate zirconate (PZT) transducers with center frequencies of 2.25 MHz (V306, Olympus Inc., MA) and 5 MHz (V310, Olympus Inc., MA). The 2.25 MHz transducer has an active diameter of 0.25 inch and the 5 MHz transducer owns an active diameter of 0.5 inch.

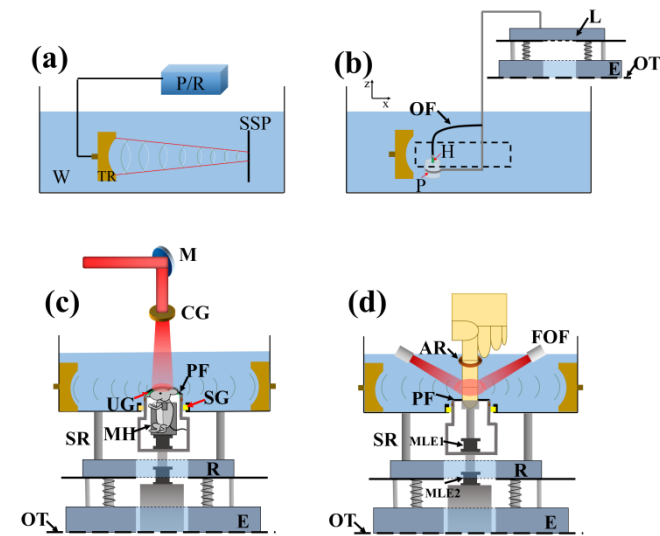


Fig. 2. Schematics of experimental systems to evaluate the performance of the transducer array, and imaging interfaces for *in vivo* mouse brain and human finger joint experiments. (a) Acoustic pulse-echo system to derive frequency response and bandwidth of the transducer. (b) Photoacoustic point-scanning system to map the acoustic distribution of the transducer. (c, d) Light delivery systems and imaging interfaces for mouse brain and human finger joint experiments. P/R: Pulse/Receiver W: water TR: PVDF transducer SSP: stainless steel plate H: hair P: background phantom E: motorized elevator stage L: motorized linear stage OF: optical fiber OT: optical table. M: mirror CG: concave lens and ground glass MH: mouse holder UG: ultrasound gel R: motorized rotator SR: support rod PF: plastic membrane SG: rubber sealing ring FOF: four-branch optical fiber bundles MLE: manual elevator stage AR: aluminum ring.

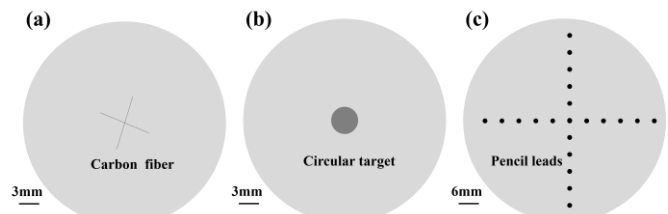


Fig. 3. Schematics of the phantoms. (a) Two  $7\text{-}\mu\text{m}$ -diameter carbon fibers are horizontally embedded in a cylindrical phantom to evaluate the lateral resolution. (b) The phantom contains a 4 mm circular target used to compare the PVDF transducer with commercial PTZ transducer. (c) 21 pencil leads are aligned in two perpendicular directions with an interval of 5 mm in a 60-mm cylindrical phantom which is used to evaluate the effective field of view.

To estimate the lateral resolution of this system, two crossed  $7\text{-}\mu\text{m}$ -diameter carbon fibers were horizontally embedded in a cylindrical tissue-mimicking background phantom, and imaged by the system. The experimental system is showed in the Figure 2c and the carbon fiber phantom is displayed in the Figure 3a. The FWHM of the imaged size of the carbon fiber was calculated as the lateral resolution of the system.

To compare the PVDF transducer with similar PZT transducers, we embedded a 4-mm circular target with an optical absorption coefficient of  $0.07\ \text{mm}^{-1}$  and an optical scattering coefficient of  $1\ \text{mm}^{-1}$  in the center of a cylindrical background phantom that had a diameter of 30 mm (Figure 3b). The phantom was imaged by the PVDF array-based system,

and the conventional 2D circular-scanning PACT system using the commercial PZT transducers, respectively. In the experiments using PZT transducers, we did a 360° circular scanning with an angular step of 2°.

To evaluate the effective imaging area of the system, we imaged a pencil-lead-embedded phantom with a diameter of 60 mm. In the background phantom, 21 pencil leads were aligned in two perpendicular directions with an interval of 5 mm (Figure 3c).

#### 4) Calibration

For array-based systems, it is required to do calibration of the raw photoacoustic signals from different elements. Before we did the phantom and *in vivo* experiments, we calibrated the system using the same sample that was used to map the acoustic distribution. We utilized a high-resolution 3D linear stage to move the carbon fiber to the center of the transducer array, recorded the raw photoacoustic signals of all elements, calibrated the phases, signal amplitudes and transducer positions in the array, and stored the calibration data for image reconstruction.

#### D. Drug-induced intracerebral hemorrhage (ICH) model and animal experiments

In addition to phantom experiments, we employed a collagenase induced cerebral hemorrhage model [41] to further evaluate the systemic performance for *in vivo* imaging. The mice, weighted around 20g, were anesthetized by i.p. of 10% chloral hydrate solution with a dose of 4 ml/kg. The hair was removed using the depilatory cream. A 1-mm hole was carefully drilled on the brain without damaging the brain tissue using an electric cranial drill. The mice were immobilized on a stereotaxic instrument and received injection of collagenase with a volume of 0.5  $\mu$ L (0.15 U/ $\mu$ L) through the hole. After the injection, the hole was sealed using the bone wax to reduce the influence on photoacoustic signals. All the animal procedures have been approved by University of Electronic Science and Technology of China (UESTC).

We present the imaging interface for mouse studies in Figure 2c. A customized holder was designed and printed by a 3D printer to immobilize the mouse during the experiments. A thorough hole with a diameter of 50 mm was opened at the bottom of the array holder. The upper end of a hollow metal cylinder with an inner diameter of 40 mm and an outer diameter of 49.9 mm was inserted into the bottom hole of the array holder, and kept motionless when the array holder rotated. To avoid water leak during the rotation, a rubber sealing ring was applied between the internal surface of the bottom hole and the outer surface of the metal cylinder. The lower end of the metal cylinder passed through the internal holes of the motorized rotator and elevator, and fixed on the optical table. The upper part of the metal cylinder was sealed using an ultrathin plastic membrane. The mouse head was attached to the membrane and vertically adjusted to select the optimal imaging plane. The gap between the membrane and mouse head was filled with ultrasound gel. The illumination light with a wavelength of 700 nm passed through a reflection mirror (GCC-101112, China Daheng Group, Inc., BJ), a Plano-concave lens and a ground

glass to form a homogenous pattern on the mouse brain. To observe the bleeding spot in depth, we carried out multiple 2D experiments in different depths with an axial scanning step of 0.8 mm. After the experiments, we extracted the entire brain and cut it into slices to identify the hemorrhagic spot.

#### E. Human finger joint experiments

Apart from the imaging interface for animal experiments, Figure 2d depicted the interface for human finger joint imaging. The emitted laser beam was split via a beam splitter (GCC-411116, China Daheng Group, Inc., BJ) and coupled into two four-branch optical fiber bundles (A4455-01, Hamamatsu Photonics K.K., Japan). All eight illumination optical fiber branches were distributed symmetrically around the finger joints with a tilted angle of 45°. To calculate the oxygen saturation, 750 nm and 830 nm were employed with the same photon density of 1 mJ/cm<sup>2</sup> on the surface of the finger joints. We recruited four healthy volunteers and carried out experiments for DIP and PIP joints of index and middle fingers, and DIP joints of ring and little fingers in both hands. We have obtained consents from all the volunteers and this study has been approved by the Institutional Review Board (IRB) office at the UESTC.

#### F. Image reconstruction and derivation of oxygen saturation

For all the experiments in this study, we employed a revised linear reconstruction algorithm named delay and sum with specific calibration data of this system. From the optical absorbing spectrum of blood, we note that deoxyhemoglobin (Hb) has a higher optical absorption than that of oxyhemoglobin (HbO) at 750 nm, while HbO has a stronger optical absorption at 830 nm. At each wavelength, both Hb and HbO contribute to the total optical absorption, which can be described by Equation 1[42].

$$\begin{bmatrix} C_{HbO} \\ C_{Hb} \end{bmatrix}_{(x,y,z)} = \left( \begin{bmatrix} \varepsilon_{HbO}(\lambda_1) & \varepsilon_{Hb}(\lambda_1) \\ \varepsilon_{HbO}(\lambda_2) & \varepsilon_{Hb}(\lambda_2) \end{bmatrix}^T \begin{bmatrix} \varepsilon_{HbO}(\lambda_1) & \varepsilon_{Hb}(\lambda_1) \\ \varepsilon_{HbO}(\lambda_2) & \varepsilon_{Hb}(\lambda_2) \end{bmatrix} \right)^{-1} \cdot \begin{bmatrix} \varepsilon_{HbO}(\lambda_1) & \varepsilon_{Hb}(\lambda_1) \\ \varepsilon_{HbO}(\lambda_2) & \varepsilon_{Hb}(\lambda_2) \end{bmatrix}^T \begin{bmatrix} \mu_a(\lambda_1) \\ \mu_a(\lambda_2) \end{bmatrix} \cdot K \quad (1)$$

Where,  $C_{Hb}$  and  $C_{HbO}$  represent the concentrations of Hb and HbO,  $\varepsilon_{Hb}$  and  $\varepsilon_{HbO}$  are the molar extinction coefficients,  $\mu_a(\lambda_1)$  and  $\mu_a(\lambda_2)$  are the true optical absorption coefficients at different wavelengths, and  $K$  is the proportionality coefficient determined by acoustic parameters. To derive the actual concentrations of Hb and HbO, a quantitative reconstruction algorithm is required. However, based on the definition of oxygen saturation in Equation 2, relative concentrations of Hb and HbO are sufficient. Hence, we assume that the reconstructed values in the image represent the relative optical absorption coefficients and calculate the relative concentrations of Hb and HbO by solving linear equations.

$$sO_{2(x,y,z)} = \frac{C_{HbO(x,y,z)}}{C_{HbO(x,y,z)} + C_{Hb(x,y,z)}} \quad (2)$$

### III. RESULTS AND DISCUSSIONS

The center frequency and bandwidth of the transducer determine the spatial resolution of the system. Figure 4a shows the raw pulse-echo response of a typical PVDF transducer. From the derived frequency response in Figure 4b, the center frequency and -6 dB bandwidth are 6.6 MHz and 95%, respectively. The normalized pulse echo response and bandwidth of all 60 elements are shown in Figure 4c. Figure 4d plots the center frequencies of the 60 transducers. Figure 4e presents the acoustic distribution map of a single PVDF transducer. As we expect, the curved shape forms a cylindrical acoustic distribution in which the acoustic pressures at the focal plane are much stronger than that of off-focus areas. The axial resolution of this system is mainly determined by the thickness of the focal plane which is estimated to be 800  $\mu\text{m}$  based on the FWHM of the axial profile shown in Figure 4f. In addition, we note that the transducer has an effective focal zone of 7 mm. Within the focal zone, the system has the same axial resolution of 800  $\mu\text{m}$ . In other areas out of the focal zone, the axial resolution will gradually deteriorate. Furthermore, the acoustic pressures in the area before the focal plane are stronger than that of the areas after the focal plane due to the acoustic attenuations in the coupling medium.

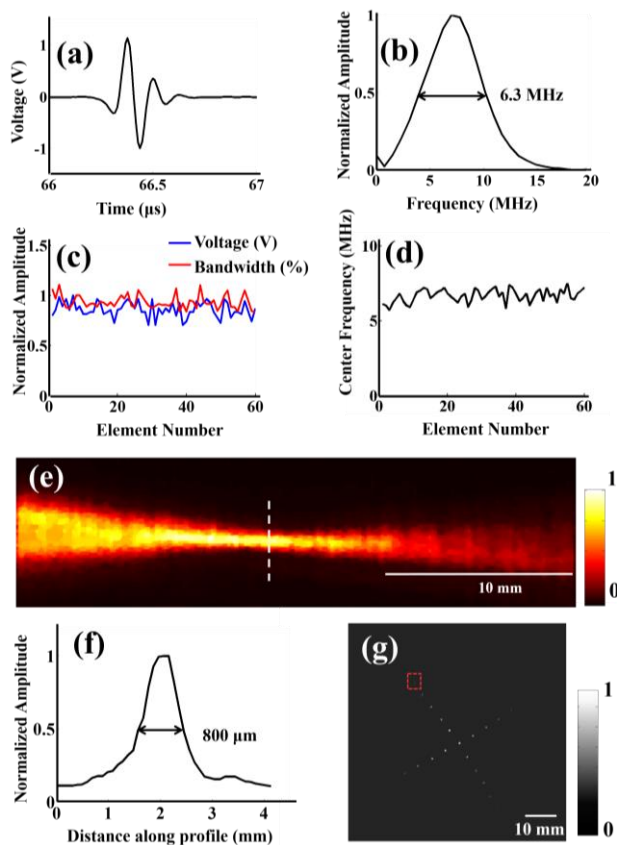


Fig. 4. Transducer and system evaluation. Pulse echo response (a) and derived frequency spectrum (b) of a single-element PVDF transducer. (c) The normalized pulse echo response and bandwidth of all 60 elements. (d) The center frequencies of all 60 transducers. (e). Measured acoustic distribution of a typical single-element PVDF transducer. (f). Axial profile of the focal plane indicated by the white dashed line in Figure 4e. (g) The phantom result of a pencil-embedded phantom to evaluate the effective imaging area of the system.

To evaluate the experimental effective imaging area of the system, we imaged a phantom embedded with pencil leads. In Figure 4g, all the pencil leads in the phantom are clearly imaged. The pencil lead indicated by a red dashed rectangle is 25 mm off the center, which represents the radius of the effective imaging area. Although the effective imaging area is sufficient to cover the entire human finger joints, the sensitivity is not homogenous over the entire area and there is slightly tangential distortion of the imaged pencil lead in the off-center areas due to the limited directivity of the transducer. It is feasible to improve the directivity of the transducer by using a negative acoustic lens and reduce the imbalanced distribution of sensitivity by considering the transducer directivity in the reconstruction algorithm [43].

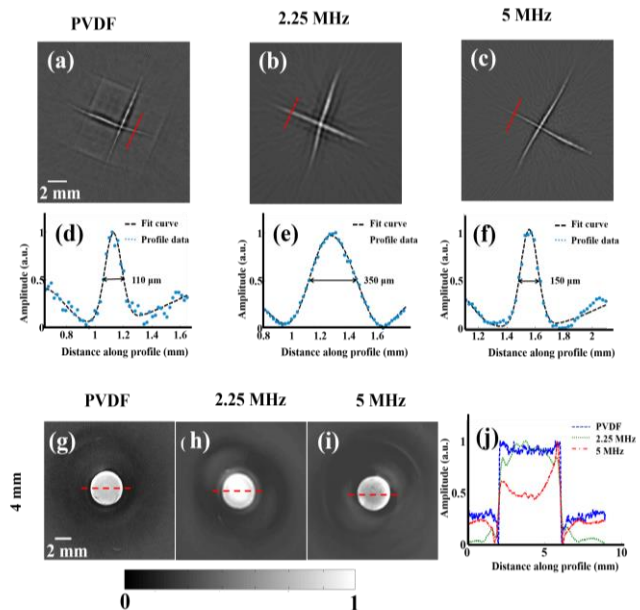


Fig. 5. Comparison of PVDF and PZT transducers. (a-c) The reconstructed images of 7  $\mu\text{m}$  carbon fibers using PVDF, 2.25 MHz and 5 MHz PZT transducers, respectively. (d-f) The corresponding normalized profiles of the red dashed lines in Figures 5a-5c, respectively. (g-i) The reconstructed images of the same 4-mm circular target using PVDF, 2.25 MHz and 5 MHz PZT transducers, respectively. (j) The corresponding normalized profiles along the red dashed lines in Figures 5g-5i.

To evaluate the lateral resolution of this system and compared it with commercial PZT transducers, we carried out phantom experiments of carbon fibers. Figures 5a-5c show the image results of two crossed carbon fibers with a diameter of 7  $\mu\text{m}$  using different transducers, and Figures 5d-5f plot the profiles of a carbon fiber along the dashed red lines in Figures 5a-5c. Given that PACT has a lateral resolution ranged from dozens of microns to hundreds of microns depending on the center frequency and bandwidth of the transducer, 7- $\mu\text{m}$  carbon fiber is small enough to be regarded as an ideal point-target. Hence, we are able to estimate the lateral resolution using the FWHM of the imaged size of a carbon fiber. The lateral resolution of the PVDF array system is estimated to be 110  $\mu\text{m}$  (Figure 5d), and systems using 2.25 MHz and 5 MHz transducers have lateral resolutions of 350  $\mu\text{m}$  (Figures 5b and 5e) and 150  $\mu\text{m}$  (Figures 5c and 5f), respectively.

In order to compare the bandwidths of these three transducers, we performed phantom experiments of circular tumor-mimicking targets with a diameter of 4 mm. As shown in Figures 5g-5i, all three transducers are able to image the target with sufficient SNR and accurate location. 5-MHz transducer provides a sharp boundary associated with high-frequency photoacoustic signals, but loses internal information related to low-frequency photoacoustic signals. 2.25-MHz transducer is able to accurately recover the inside structure of the target, however, the boundary is blur. Comparing with two PZT transducers, PVDF transducer array offers both a sharp boundary and sufficient internal structures as shown in Figure 5j which plot the profiles along the dashed red lines in Figures 5g-5i.

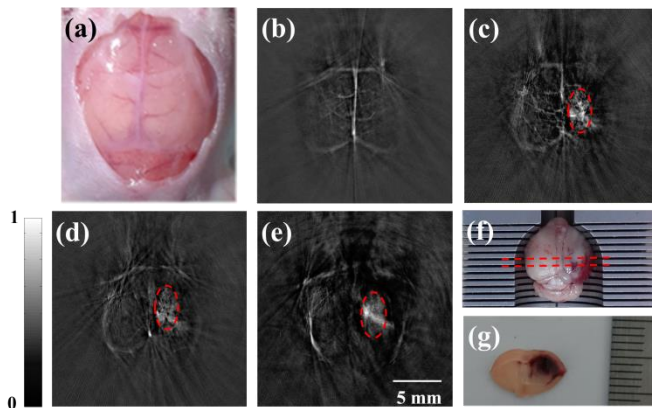


Fig. 6. Experimental results of a mouse brain with collagenase induced cerebral hemorrhage. (a) Photograph of the mouse brain without scalp. (b) *In vivo* imaging result of the mouse brain before the injection of collagenase. (c, d, e) The images of the mouse brain in different depths after the injection of collagenase. (f) Photograph of the extracted brain after the experiment. (g) A typical cross-sectional slice of the extracted brain along the dashed red lines in Fig. 6f.

Before the experiments of human finger joints, we carried out *in vivo* experiments of mouse brain to further test the performance of this system. Figure 6a shows a photograph of the mouse brain with removal of the scalp after the experiment, and Figure 6b presents the corresponding photoacoustic image. From the comparison, we can observe both major and small blood vessels non-invasively using the proposed system with sufficient resolution and SNR. Furthermore, we developed an intracerebral hemorrhage model in the brain with injection of collagenase. We re-imaged the mouse brain in multiple depths at 8 hours post the injection. In Figure 6c, we observe the bleeding spot indicated by the dashed red circle, and find that small blood vessels disappear and several major blood vessels become discontinued due to serious bleeding in the brain. Figure 6d and 6e show the images in 2 mm and 4 mm under the brain surface, in which we still clearly observe the bleeding spot. After the experiments, we extracted the entire brain and cut it into slices to confirm the successful induce of the hemorrhage and identify the actual position of the bleeding spot. As shown in Figure 6f and 6g, the spatial position of the bleeding spot is consistent with our image results.

We performed pre-clinical experiments of human finger joints with multispectral strategy to recover both structural and

functional information of blood vessels in the DIP and PIP joints of healthy volunteers. Figures 7a and 7c show the images of DIP and PIP joints of the index finger. Figure 7b and 7d display the images of bleed vessels in DIP and PIP joints of the middle finger. It is challenging to image the PIP joints of ring and little fingers due to the limitations of the imaging interface. In addition to the structures, we derived the oxygen saturation of blood vessels in DIP joints of ring and little fingers and overlapped the data with structural images in Figure 7e and 7f. Through using structural and functional parameters such as vessel size, vessel density, and oxygen saturation, it is feasible to develop a multi-parameter based diagnostic method for early-stage arthritis patients in clinics.

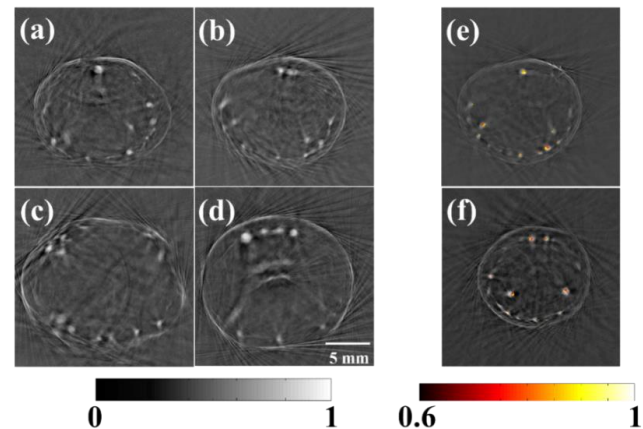


Fig. 7. PA imaging results of a healthy female fingers. (a, c) PA images of blood vessels in the DIP and PIP joints of an index finger. (b, d) PA images of blood vessels in the DIP and PIP joints of a middle finger. (e, f) Structural images overlapped with oxygen saturation of blood vessels in DIP joints of ring and little fingers.

#### IV. CONCLUSIONS

In summary, we introduced the design, fabrication, and evaluation of a PACT system based on a 60-element curved ultrasonic transducer array fabricated by PVDF. From phantom experiments, the system owns a lateral of 110  $\mu\text{m}$ , an axial resolutions of 800  $\mu\text{m}$ , and an effective imaging area with a diameter of 50 mm. Through experimental comparison, the PVDF transducer has a better performance in bandwidth compared with commercial transducers. Furthermore, we successfully demonstrated the feasibility of deriving morphological and functional parameters of blood vessels in human finger joints, which are closely associated with the early development of arthritis. Before the system is ready for actual clinical evaluation, we still need to improve it in the following aspects. 1) We are able to develop a multi-layer PVDF transducer array with improved bandwidth and sensitivity in the next generation. 2) Although we developed two-stage amplifiers at  $\sim 48$  dB, the magnification is still not high enough. Now, we are investigating a new two-stage low-noise amplifier with a magnification of 80 dB, which will significantly improve the SNR of raw signals. 3) To achieve real-time imaging, a 60-channel data acquisition system is required. 4) We observed some artifacts in the reconstructed images of finger joints, which are caused by the strong acoustic reflection of bones in

the finger joints and inhomogeneous acoustic velocities over the entire reconstruction area. To remove these artifacts, a more complicated reconstruction algorithm with consideration of all the factors is required. 5) The pitch of the transducer array is relatively large, which may cause potential grating lobe artifacts in the regions away from the center. It is feasible to reduce the artifacts by adding more elements and combing the reconstruction algorithm with new image processing methods such as compress sensing/total variation in the reconstruction [44], [45].

## REFERENCES

- [1] S. B. Abramson, M. Attur and Y. Yazici, "Prospects for disease modification in osteoarthritis," *Nat. Clin. Pract. Rheumatol.*, vol. 2, no. 6, pp. 304-312, Jun. 2006.
- [2] G. A. Schellekens *et al.*, "The diagnostic properties of rheumatoid arthritis antibodies recognizing a cyclic citrullinated peptide," *Arthritis Rheum.*, vol. 43, no. 1, pp. 155-163, Jan. 2000.
- [3] E. Calvo *et al.*, "High-resolution MRI detects cartilage swelling at the early stages of experimental osteoarthritis," *Osteoarthritis Cart.*, vol. 9, no. 5, pp. 463-472, Jul. 2001.
- [4] D. Kane *et al.*, "A prospective, clinical and radiological study of early psoriatic arthritis: an early synovitis clinic experience," *Rheumatology*, vol. 42, no. 12, pp. 1460-1468, Dec. 2003.
- [5] A. H. van der Helm-van Mil *et al.*, "Antibodies to citrullinated proteins and differences in clinical progression of rheumatoid arthritis," *Arthritis Res. Ther.*, vol. 7, no. 5, pp. R949-R958, Jun. 2005.
- [6] A. Hammond, A. Young and R. Kidao, "A randomised controlled trial of occupational therapy for people with early rheumatoid arthritis," *Ann. Rheum. Dis.*, vol. 63, no. 1, pp. 23-30, Jan. 2004.
- [7] R. B. Landewé *et al.*, "COBRA combination therapy in patients with early rheumatoid arthritis," *Arthritis Rheum.*, vol. 46, no. 2, pp. 347-356, Feb. 2002.
- [8] F. W. Roemer *et al.*, "Advances in imaging of osteoarthritis and cartilage," *Radiology*, vol. 260, no. 2, pp. 332-354, Aug. 2011.
- [9] J. A. Tyler *et al.*, "Detection and monitoring of progressive degeneration of osteoarthritic cartilage by MRI," *Acta Orthoped. Scand.*, vol. 66, no. 266 Suppl, pp. 130-138, Jul. 2009.
- [10] S. L. Myers *et al.*, "Experimental assessment by high frequency ultrasound of articular cartilage thickness and osteoarthritic changes," *J. Rheumatol.*, vol. 22, no. 1, pp. 109-116, Feb. 1995.
- [11] G. Spahn, G. Felmet and G. O. Hofmann, "Traumatic and degenerative cartilage lesions: arthroscopic differentiation using near-infrared spectroscopy (NIRS)," *Arch. Orthop. Trauma. Surg.*, vol. 133, no. 7, pp. 997-1002, May 2013.
- [12] Z. Yuan *et al.*, "Tomographic x-ray-guided three-dimensional diffuse optical tomography of osteoarthritis in the finger joints," *J. Biomed. Opt.*, vol. 13, no. 4, Aug. 2008, Art. no. 044006.
- [13] A. H. Hielscher *et al.*, "Sagittal laser optical tomography for imaging of rheumatoid finger joints," *Phys. Med. Biol.*, vol. 49, no. 7, pp. 1147-1163, Mar. 2004.
- [14] R. A. Shaw *et al.*, "Arthritis diagnosis based upon the near-infrared spectrum of synovial fluid," *Rheumatol. Int.*, vol. 15, no. 4, pp. 159-165, Nov. 1995.
- [15] L. Xi *et al.*, "Design and evaluation of a hybrid photoacoustic tomography and diffuse optical tomography system for breast cancer detection," *Med. Phys.*, vol. 39, no. 5, pp. 2584-2594, Apr. 2012.
- [16] B. Brooksby *et al.*, "Imaging breast adipose and fibroglandular tissue molecular signatures by using hybrid MRI-guided near-infrared spectral tomography," *Proc. Natl. Acad. Sci. USA*, vol. 103, no. 23, pp. 8828-8833, Jun. 2006.
- [17] L. V. Wang and S. Hu, "Photoacoustic tomography: in vivo imaging from organelles to organs," *Science*, vol. 335, no. 6075, pp. 1458-1462, Mar. 2012.
- [18] L. V. Wang, "Multiscale photoacoustic microscopy and computed tomography," *Nature Photon.*, vol. 3, no. 9, pp. 503-509, Aug. 2009.
- [19] L. Yao, L. Xi and H. Jiang, "Photoacoustic computed microscopy," *Sci. Rep.*, vol. 4, May 2014, Art. no. 04960.
- [20] X. Wang, D. L. Chamberland and D. A. Jamadar, "Noninvasive photoacoustic tomography of human peripheral joints toward diagnosis of inflammatory arthritis," *Opt. Lett.*, vol. 32, no. 20, pp. 3002-3004, Oct. 2007.
- [21] L. Xi *et al.*, "Evaluation of breast tumor margins in vivo with intraoperative photoacoustic imaging," *Opt. Express*, vol. 20, no. 8, pp. 8726-8731, Apr. 2012.
- [22] Y. Sun, E. Sobel and H. Jiang, "Quantitative three-dimensional photoacoustic tomography of the finger joints: an in vivo study," *J. Biomed. Opt.*, vol. 14, no. 6, Nov. 2009, Art. no. 064002.
- [23] L. Xi and H. Jiang, "High resolution three-dimensional photoacoustic imaging of human finger joints in vivo," *Appl. Phys. Lett.*, vol. 107, Aug. 2015, Art. no. 063701.
- [24] L. Xi and H. Jiang, "Integrated photoacoustic and diffuse optical tomography system for imaging of human finger joints in vivo," *J. Biophotonics*, vol. 9, no. 3, pp. 213-217, Oct. 2015.
- [25] Z. Deng and C. Li, "Noninvasively measuring oxygen saturation of human finger-joint vessels by multi-transducer functional photoacoustic tomography," *J. Biomed. Opt.*, vol. 21, no. 6, May 2016, Art. no. 061009.
- [26] X. Wang *et al.*, "Noninvasive laser-induced photoacoustic tomography for structural and functional in vivo imaging of the brain," *Nat. Biotechnol.*, vol. 21, no. 7, pp. 803-806, Jul. 2003.
- [27] J. Gamelin *et al.*, "Curved array photoacoustic tomographic system for small animal imaging," *J. Biomed. Opt.*, vol. 13, no. 2, Apr. 2008, Art. no. 024007.
- [28] J. Gamelin *et al.*, "A real-time photoacoustic tomography system for small animals," *Opt. Express*, vol. 17, no. 13, pp. 10489-10498, Jun. 2009.
- [29] D. Yang *et al.*, "Fast full-view photoacoustic imaging by combined scanning with a linear transducer array," *Opt. Express*, vol. 15, no. 23, pp. 15566-15575, Nov. 2007.
- [30] L. Xiang *et al.*, "Noninvasive real time tomographic imaging of epileptic foci and networks," *NeuroImage*, vol. 66, pp. 240-248, Feb. 2013.
- [31] B. Wang *et al.*, "Photoacoustic tomography system for noninvasive real-time three-dimensional imaging of epilepsy," *Biomed. Opt. Express*, vol. 3, no. 6, pp. 1427-1432, May 2012.
- [32] H. P. Brecht *et al.*, "Whole-body three-dimensional optoacoustic tomography system for small animals," *J. Biomed. Opt.*, vol. 14, no. 6, Nov. 2009, Art. no. 064007.
- [33] R. A. Kruger *et al.*, "Photoacoustic angiography of the breast," *Med. Phys.*, vol. 37, no. 11, pp. 6096-6100, Nov. 2010.
- [34] P. van Es *et al.*, "Initial results of finger imaging using photoacoustic computed tomography," *J. Biomed. Opt.*, vol. 19, no. 6, Jun. 2014, Art. no. 060501.
- [35] C. Lutzweiler *et al.*, "Real-time optoacoustic tomography of indocyanine green perfusion and oxygenation parameters in human finger vasculature," *Opt. Lett.*, vol. 39, no. 14, pp. 4061-4064, Jul. 2014.
- [36] G. Xu *et al.*, "Photoacoustic and ultrasound dual-modality imaging of human peripheral joints," *J. Biomed. Opt.*, vol. 18, no. 1, Jan. 2013, Art. no. 010502.
- [37] S. A. Ermilov *et al.*, "Laser optoacoustic imaging system for detection of breast cancer," *J. Biomed. Opt.*, vol. 14, no. 2, Mar. 2009, Art. no. 024007.
- [38] X. Li *et al.*, "Integrated diffuse optical tomography and photoacoustic tomography: phantom validations," *Biomed. Opt. Express*, vol. 2, no. 8, pp. 2348-2353, Aug. 2011.
- [39] S. Manohar *et al.*, "Photoacoustic mammography laboratory prototype: Imaging of breast tissue phantoms," *J. Biomed. Opt.*, vol. 9, no. 6, pp. 1172-1181, Nov. 2004.
- [40] J. Tang *et al.*, "Noninvasive high-speed photoacoustic tomography of cerebral hemodynamics in awake-moving rats," *J. Cereb. Blood Flow Metab.*, vol. 35, no. 8, pp. 1224-1232, Jun. 2015.
- [41] G. A. Rosenberg *et al.*, "Collagenase-induced intracerebral hemorrhage in rats," *Stroke*, vol. 21, no. 5, pp. 801-807, May 1990.
- [42] J. Tang *et al.*, "Wearable 3-D photoacoustic tomography for functional brain imaging in behaving rats," *Sci. Rep.*, vol. 6, May 2016, Art. no. 25470.
- [43] Z. Yuan and H. Jiang, "Three-dimensional finite-element-based photoacoustic tomography: reconstruction algorithm and simulations," *Med. Phys.*, vol. 34, no. 2, pp. 538-546, Feb. 2007.
- [44] C. H. Chiu and M. L. Li, "Compressive-Sensing Like Grating-Lobe Suppressed Image Reconstruction for Photoacoustic Linear Array Imaging," in *Proc. IEEE-IUS*, Chicago, IL, USA, 2014, pp. 1277-1279.
- [45] L. Yao and H. Jiang, "Enhancing finite element-based photoacoustic tomography using total variation minimization," *Appl. Opt.*, vol. 50, no. 25, pp. 5031-5041, Sep. 2011.



**Na Huang** received the B.S. degree from the University of Electronic Science and Technology of China (UESTC), Chengdu, Sichuan, China, in 2015. She is currently working toward the M.S. degree in Multi-Functional Optical Imaging Lab (MFOIL) at UESTC. Her research focuses on developing array-based photoacoustic tomography systems.



**Xianbing Zou** received the B.E. degree in physics from Gannan Normal University, Ganzhou, China, in 1995, and M.E. degree from University of Electronic Science and Technology of China (UESTC), Chengdu, China, in 1998. He is now an associate professor of electronics and communication engineering at UESTC. His current research interests include analog circuits and antenna technology in wireless communication.



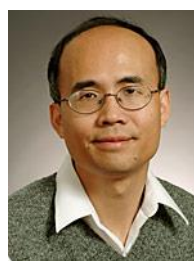
**Ming He** received the B.S. degree from Nanchang Hangkong University, Nanchang, Jiangxi, China, in 2016. He is currently working in the Multi-Functional Optical Imaging Lab (MFOIL) at UESTC. His research interests include photoacoustic tomography imaging and applications.



**Lei Yao** received the B.S. degree and Ph.D. degree in mechanics and mechanical engineering from the University of Science and Technology of China, in 1999 and 2005, respectively. He is a professor of physical electronics with the University of Electronic Science and Technology of China. His research focuses on developing reconstruction algorithm in photoacoustic imaging technologies and their applications to biomedicine.



**Haosheng Shi** received the B. S. degree in vacuum electronics technology from UESTC in 2014. He is studying for M.S. degree in communication and information system from UESTC.



**Huabei Jiang** is a professor in the Department of Medical Engineering at the University of South Florida. He received his PhD at Dartmouth College (1995). He is a pioneer in the field of near-infrared diffuse optical tomography, fluorescent molecular tomography and photoacoustic tomography. He has been named a Fellow of the Optical Society of America (OSA) and the International Society for Optics and Photonics (SPIE).



**Yuan Zhao** received the B.S. degree at School of Physical Electronics in the University of Electronic Science and Technology of China, Chengdu, Sichuan, China, in 2014. He is now a Ph.D. student in and His research focuses on developing thermoacoustic imaging technologies and its applications to translational medicine.



**Lei Xi** received his bachelor degree from Huazhong University of Science and Technology (2007) in optics, and finished his doctoral and post-doctoral training in the Department of Biomedical Engineering at the University of Florida majored in biophotonics. Then, he joined University of Electronic Science and Technology of China (UESTC) as a professor. Now, he is hosting the multifunctional optical imaging lab (MFOIL) in UESTC and focusing on developing novel optical imaging techniques for different biomedical and clinical researches.



**Man Lu** received the B.S. degree in medical Imaging from North Sichuan Medical College, Nanchong, China in 1993, and M.S. and Ph.D. degree in medical Imaging from West China School of Medicine, Chengdu, China, in 2006 and 2012, respectively. Her research focuses on musculoskeletal ultrasound, interventional ultrasound, and gastrointestinal ultrasound.